LSM-YSZ CATHODES WITH REACTION-INFILTRATED NANOPARTICLES

Chun Lu[1], Tal Z. Sholklapper[1, 2], Craig P. Jacobson[1], Steven J. Visco[1],

and Lutgard C. De Jonghe[1, 2]

[1] Materials Sciences Division

Lawrence Berkeley National Laboratory

Berkeley, CA 94720

and

[2] Materials Science and Engineering Department

University of California at Berkeley

Berkeley CA 94720

ABSTRACT

To improve the LSM-YSZ cathode performance of intermediate temperature solid oxide fuel cells (SOFCs), $Sm_{0.6}Sr_{0.4}CoO_{3-\delta}$ (SSC) perovskite nanoparticles are incorporated into the cathodes by a reaction-infiltration process. The SSC particles are ~20 to 80nm in diameter, and intimately adhere to the pore walls of the pre-formed LSM-YSZ cathodes. The SSC particles dramatically enhance single-cell performance with a 97%H_2+3%H_2O fuel, between 600^oC and 800^oC. Consideration of a simplified TPB (triple phase boundary) reaction geometry indicates that the enhancement may be attributed to the high electrocatalytic activity of SSC for electrochemical reduction of oxygen in a region that can be located a small distance away from the strict triple phase boundaries. The implication of this work for developing high-performance electrodes is also discussed.

INTRODUCTION

For practical SOFC cathodes, the selected materials must be chemically and structurally stable, and be compatible with adjacent cell components, not only under operation conditions, but also at the high temperatures where SOFC membranes are fabricated. The cathode must be catalytically active to promote the electrochemical reduction of oxygen, and have a high electronic conductivity to exhibit a low polarization resistance (1, 2). Since $La_{1-x}Sr_xMnO_{3-\delta}$ (LSM)-YSZ (yttria stabilized zirconia) composites reasonably meet these criteria, they are the most popular cathode material used in SOFCs operated at temperatures above 800^{o}C.

To reduce costs, lowering of the SOFC operating temperatures has been widely pursued to expand the materials selection, to suppress the degradation of SOFC components, and consequently to extend cell lifetime (3-7). Unfortunately, with decreasing temperatures the low oxygen ion diffusivity and reduced catalytic activity of LSM tends to limit cell performance (8, 9). Noble metals particles, including Ru and Pt, have been incorporated in cathodes to improve performance (8, 10) but, from a practical point of view, their prohibitive cost and tendency to coarsen at high temperatures make this approach unattractive. Recently, cobalt oxide particles were infiltrated into LSM-YSZ cathodes, significantly raising cathode performance (11-13). This suggests the general possibility of directly introducing catalytically active materials into pre-formed LSM-YSZ cathodes to enhance their activity. Compared to LSM, the $Sm_{0.6}Sr_{0.4}CoO_{3-\delta}$ (SSC) perovskite is a superior electrocatalyst for oxygen-reduction reaction because of its mixed ionic-electronic conduction properties (14-16). We developed a reaction-infiltration method that produces nanosize SSC

particles in the pores of the pre-formed LSM-YSZ cathodes. The morphologies of the resulting cathodes and the effect of SSC addition on cell performance are reported.

EXPERIMENTAL

A reaction-infiltration method was developed to deposit nano particles (SSC, LSM, $La_{0.8}Sr_{0.2}FeO_{3-\delta}$ (LSF)) into porous LSM-YSZ electrodes. As a base line, aqueous precursor solutions for these materials, containing nitrates in corresponding ratios as well as urea ($CO(NH_2)_2$), were heated at 90^{o}C for 2hrs before firing at 800^{o}C for 2hrs. The decomposition products were then examined using a (Siemens D-500) diffractometer with CuK_α radiation in the 2θ range from 20^o to 80^o.

Single SOFC cells were fabricated by tape casting (6). Nickel oxide (NiO; J. T. Baker) and YSZ (Tosoh-Zirconia; TZ-8Y) powders in a 50:50wt% ratio were thoroughly mixed in water with Duramax D3005 as the dispersant. Duramax B1000 and HA-12 binders were then added to form the NiO-YSZ slurry. After evaporation of excessive water, the slurry was tape-cast onto a Mylar film, and dried at ambient temperature. The green tape was then cut into circular discs with a diameter of about 4cm, and preheated at 1100^{o}C for 2hrs. A thin layer of YSZ powder was deposited by an aerosol spray method (7), and the resulting bi-layer was sintered at 1400^{o}C, for 4hrs, to obtain a dense YSZ electrolyte. A $La_{0.65}Sr_{0.3}MnO_{3-\delta}$ (Praxair Specialty Ceramics):YSZ (50:50wt%) cathode with an active area of 1cm^2 was then deposited on the electrolyte via the aerosol spray method, and the samples were fired again, at 1150^{o}C, for 1hr, in air. Symmetric cells (cathode/electrolyte/cathode) were also prepared using the aerosol spray method (7). For these cells, LSM-YSZ electrodes were sprayed on both sides of a thick YSZ disc (~0.7mm), and subjected to the identical treatment described above. The porous cathodes

were saturated with a 0.7M nitrate/urea precursor solution, and heat-treated using the same heating schedule as for the *ex-situ* preparation of the SSC. In this process, the pores may be regarded as micro-reaction vessels, in which the pore walls act as the heterogeneous nucleation sites for precipitate formation. Related urea methods for coating SiC particles and hollow glass spheres with oxides, exploiting heterogeneous nucleation, were employed in several other instances (17, 18).

Platinum current collectors were placed on the electrodes of both symmetric and single cells, and these samples were fired at 800^{o}C for 2hrs. For the symmetric cells, the electrode polarization resistance was measured in air at open circuit (OCV), using a Solartron 1260 frequency response analyzer with a Solartron 1286 electrochemical interface. Completed single SOFC membranes were sealed onto an alumina tube with Aremco-516 cement. Cell current/voltage (I-V) for 97%H_2+3%H_2O as the fuel, and air as the oxidant were collected using LabView software, and cell impedance spectra were obtained as well. The cathode morphologies were characterized with a JEOL FE-scanning electron microscope and examined in a PHILIPS CM200 transmission electron microscope. Based on the SEM observations of single cells, the cell component thickness was ~300μm, ~10μm, and ~30μm for the anode, the electrolyte, and the cathode, respectively.

RESULTS

Urea is added into the aqueous nitrate precursor solutions to facilitate the formation of the perovskite SSC phase at 800^{o}C. At this temperature, adverse reactions between SSC and YSZ that can occur at high temperatures (14) are avoided. Fig. 1 shows the XRD patterns of the decomposition products from the nitrate precursor solutions with and

without urea, after heating at 800^{o}C for 2hrs. The characteristic x-ray peaks in Fig. 1a indicate that the SSC perovskite phase did not form as the decomposition product of the nitrate precursor solution. In contrast, with the addition of urea, the perovskite SSC phase becomes the predominant decomposition product, as evident in Fig. 1b. The detailed role of urea in this change has yet to be identified; it probably serves as a precipitation and complexing agent to form intimately mixed intermediate species, only requiring low-temperature heating to produce the desired phases (19-21).

The SSC particles that formed in the pores were examined with EDX (energy dispersive x-ray analysis) in the transmission electron microscope. The inset in Fig. 2 shows a particle of ~60nm in the cathode produced by the reaction-infiltration process. The EDX spectrum contains O, La, Sm, Sr, Zr, Ar, Mn, Co and Y. Besides the contribution from supporting LSM, YSZ and Ar implanted during ion-mill processing to prepare the TEM specimen, the presence of Sm, Co strongly indicates the formation of nanosized SSC particles instead of the individual metal oxides, consistent with the *ex-situ* procedure.

Fig. 3 is a SEM image of a porous LSM-YSZ cathode with infiltrated SSC nano particles. The infiltrated SSC particles are ~20 to ~80nm, and appear to be well bonded to the pore walls of the LSM-YSZ network. Interestingly, most of particles are isolated from each other. The insert in Fig. 3 shows the SSC particles after heating at 700^{o}C for 750hrs; the particles appears to be about 40 to 90nm and, as expected, show little if any evidence of coarsening. This is an encouraging result, since morphological stability is an important requirement for the effectiveness of the process.

The reaction-infiltrated SSC nanoparticles in LSM-YSZ cathodes substantially enhance the cell performance, as shown in Fig. 4. At 600^{o}C the cell OCVs with the

97%H_2 + 3%H_2O fuel are ~1.1V, indicating that the cells were well sealed. The SSC reaction-infiltration almost doubles cell performance, and the cell maximum power density (MPD) increases from 80mW/cm^2 to 153mW/cm^2. Furthermore, the SSC addition noticeably decreases the initial curvature of the I-V plots at low current densities. This decrease can be further substantiated by the impedance measurement data shown in Fig. 5. At 600^{o}C the cell total resistance (R_t) (the intercept of the impedance spectrum on the real axis at low frequency) declines from ~9.9 to 3.3Ω·cm^2 when SSC is included into the LSM-YSZ cathode. The enhancement effect persisted up to 800^{o}C. The performance improvement factor is calculated as the percentage of MPD (maximum power density) increase and is ~ 91%, 67%, 44% and 38% for 600^{o}C, 650^{o}C, 700^{o}C and 800^{o}C, respectively. The relative improvement diminishes when the cell operating temperature is raised, which may be attributed the increasing catalytic activity and oxygen ion diffusivity of LSM itself with temperature. However, even at 800^{o}C the SSC particles in the cathode still enhance the performance.

DISCUSSION

The cell-performance enhancement originates in the improvement of the LSM-YSZ cathode upon the introduction of the SSC nanoparticles. Fig. 6 displays the impedance spectra of LSM-YSZ/YSZ/LSM-YSZ symmetric cells without and with infiltrated catalyst at 600^{o}C. All AC impedance spectra show a relatively small high-frequency branch (HFB) and a dominant low-frequency branch (LFB). The cell ohmic resistance in the spectra is truncated for comparison, and the cathode polarization resistance (R_p) is directly determined from the spectra as illustrated (22). With the infiltrated SSC

nanoparticles in the cathode, both the HFB and LFB are largely diminished so that R_p is reduced from ~19.8 to 8.5Ω·cm^2 at 600^{o}C.

Where LSM contacts the YSZ, a triple phase boundary (TPB) is formed, in the presence of a gas phase. Important in the functioning of such junction is the extent to which the relevant reactions can occur some distance away from the strict triple junction. Numerous advanced studies on electrode behaviors have been carried out to date (16, 23-26). The oxygen reduction processes in fuel cell cathodes were recently reviewed by Adler (9), yet understanding of TPB processes is still incomplete, due to the complex competition of various transport paths and interface mechanisms.

A qualitative assessment of the relative effects of some transport parameters on the effectiveness of cathode may be obtained from a very simplified model for an extended, modified TPB, provided constancy of the microstructure. The extended TPB is sketched in Fig. 7, and can be related to a model described by Kawada *et al*. (27). It considers an LSM grain, of length 2L, in electronic contact with the current collector, between two grains of the YSZ skeleton, with the TPB extending over the LSM grain surface. It is then assumed that this extended TPB may be divided in two zones, Zone 1 of extent δ, where the unaffected surface exchange limits the reaction rate, and Zone 2**,** extending to L where, after infiltration, an enhanced surface reaction rate prevails. The total extended TPB current, ignoring all dependences on current density, could be regarded as the series resistances of the Zones 1 and 2. It is useful to define reaction and transport resistances for such simplified geometry. R^{ox} (in Ωcm) could stand for the oxygen ion diffusion "resistance", ignoring the details of the transport geometry, while R_1^S and R_2^S (in Ωcm^2) symbolize the interface reaction resistances in Zones 1 and 2, respectively.

In such simplified model, the total relative TPB conductivity, ρ, will be proportional to

$$\rho=\rho_\delta + \rho_L \qquad \text{Eqn.1}$$

where

$$\rho_\delta=\delta/ R_1^S \qquad \text{Eqn.2}$$

and

$$\rho_L = \int_\delta^L \frac{1}{R_2^S + R_o^{ox}} dx = \frac{1}{R_o^{ox}} \mathbf{ln}(\frac{R_o^{ox} L + R_2^S}{R_o^{ox}\delta + R_2^S}) \qquad \text{Eqn.3}$$

where the total TPB flux can be take to proportional to the total conductivity.

With the usual expressions for the conductivities, R_o^{ox} and R^s may be taken to be related to D_o^{ox}, the bulk oxygen ion self-diffusion coefficient, and to the surface exchange coefficient, k^s. The relationships between D_o^{ox}, k^s and L_c, the critical length above which diffusion resistance dominates, were developed by Steele (28), and have been reviewed by Gellings and Bouwmeester (29). These considerations led to $D_o^{ox}/k^s = L_c$ and consequently to $R^s / R_o^{ox} = L_c$.

In the one extreme, for a fully impeded surface reaction, *i.e.* $R_2^S \to \infty$, ρ_L (Eqn.3) becomes simply proportional to $(L-\delta)/R_2^S$, as expected, since $\ln[\frac{R_o^{ox} L + R_2^s}{R_o^{ox}\delta + R_2^s}] \to \frac{R_o^{ox}(L-\delta)}{R_2^s}$. In the other extreme, for very effective catalysis, corresponding to $R_2^S << R_o^{ox}\delta$, ρ_L becomes proportional to $\frac{1}{R_o^{ox}} \mathbf{ln}(\frac{L}{\delta})$, *i.e.* to the oxygen diffusion coefficient, as it should. Enhanced catalysis by dispersed nanoparticles adhering

to the pore walls, beginning some small distance δ away from the strict TPB, can thus be effective only between the relative limits $\frac{L-\delta}{R_2^s}$ and $\frac{1}{R_x^{ox}}\mathbf{ln}(\frac{L}{\delta})$, corresponding to the high and the low interface resistance conditions in Zone 2, if it is assumed that the surface reaction rate in Zone 1 and the oxygen diffusion rate are invariant. The result is, of course, sensitive to the choice of δ. If δ is smaller, then the range of effectiveness can become larger, while the opposite prevails if δ is larger.

A plot of $R_o^{ox}\rho = \frac{R_o^{ox}}{R_1^s}\delta + \mathbf{ln[(}L + \frac{R_2^S}{R_o^{ox}}\mathbf{)/(}\delta + \frac{R_2^S}{R_o^{ox}}\mathbf{)]}$ in relative units *versus* $\log[\frac{R_2^S}{R_o^{ox}}\text{(cm)}]$ is shown in Fig. 8, for assumed values of $\delta=10^{-3}$μm and L=1μm. It may be argued that for LSM $\delta \approx L_c = \frac{R_1^s}{R_o^{ox}}$, so that ρ_δ would be about 1 (with the present definitions ρ would have units of Ω^{-1}). It is clear from this graph that to allow for a factor of 2 increase in the TPB performance, as experimentally observed here, while keeping R_o^{ox} constant, the corresponding starting value of $\frac{R_1^s}{R_o^{ox}} = L_c$ would have to be significantly higher than 10^{-5}cm, about 2 orders of magnitude higher than the $2*10^{-7}$ cm - the value of L_c derived by Carter *et al*. (30) for LSM at about 700°C, using the measured oxygen bulk self-diffusion coefficient and surface exchange coefficient. This implies an inconsistency with the model of more than 2 orders of magnitude. The difference in the L_c that makes the dispersed catalyst effective, and the L_c values cited by Carter *et al.* are not readily reconciled, unless it is assumed that for LSM the actual oxygen diffusion rates are substantially higher than oxygen ion self diffusion rates

derived from tracer measurements, or that the surface reaction resistances are much larger than predicted from the k^s for LSM. Recent work by Horita *et al*. (31, 32) indeed suggests that the oxygen transport for LSM is more extensive than suggested by the oxygen self diffusion, leading to active surfaces of about 0.5μm away from the strict TPB. It is also clear that to enhance further the TPB performance, enhanced oxygen ion transport should accompany enhanced surface reaction rates, since nothing more can by gained by further enhancing catalysis in Zone 2. Lowering the surface reaction resistance in Zone 1, such as by surface alloying, however, can remain effective, up to the gas transport limit.

This study demonstrates that the performance of LSM-YSZ cathodes at intermediate temperatures can be improved substantially by decorating the pore walls with nanoparticles providing supplemental catalytic functions. These nanoparticle catalysts need not be confined to the strict TPB to be effective. The critical length concept, however, by itself is not a useful parameter for predicting the effectiveness of an extended TPB, since a large L_c can derive from either a high oxygen diffusion rate or a low surface reaction rate, and thus does not relate directly to TPB resistance. The total TPB resistance is, however, within limits, approximately proportional to the oxygen diffusion rate, and to a function of the L_c, as follows form Eqn. 3.

The choice of nanoparticle catalyst is not limited to SSC but should extend to other catalyst oxides that possess substantially higher catalytic activity. For example, as shown in Fig.6, replacing SSC with LSF nanoparticles in the LSM-YSZ cathodes leads to a similar beneficial result that is absent for LSM nanoparticle infiltration. It is therefore plausible that the reaction-infiltration concept can be exploited broadly in the engineering of high-performance electrodes.

CONCLUSIONS

It has been demonstrated that composite cathodes can be made to operate more effectively by reaction-infiltration of dispersed nanocatalysts that need not be fully confined to the strict TPBs. Specifically, in this study conventional LSM-YSZ cathodes have been modified by the reaction-infiltration of SSC nanoparticles, using a process that does not exceed 800^{o}C. Microstructural examinations showed extended stability of the SSC particles at least at 700^{o}C. Electrochemical characterization of single cells shows that the SSC nanoparticles dramatically increase the cell power densities between 600^{o}C and 800^{o}C. A simplified extended TPB model suggests that the enhancement by the dispersed nanocatalysts involves an oxygen ion transport rate for LSM that is significantly higher than expected from the bulk oxygen ion self diffusion in the LSM.

ACKNOWLEDGEMENTS

This work was supported by the U. S. Department of Energy, through the National Energy Technology Laboratory. Dr. Xiao-Feng Zhang is acknowledged for the TEM analysis, carried out at the LBNL NCEM.

REFERENCES

1. N. Q. Minh and T. Takahashi, *Science and Technology of Ceramic Fuel Cells*, p. 117, Elsevier Science Pub. Co. (1995).

2. H. Yokokawa, T. Horida, in *High Temperature Solid Oxide Fuel Cells*, S. C. Singhal and K. Kendall editors, p.136, Elsevier Advanced Technology, Oxford, UK (2003).

3. K. Huang, R. Tichy, J. B. Goodenough and C. Milliken, *J. Am. Ceram. Soc.*, **81** (10) 2581 (1998).

4. R. Doshi, V. Richards, J. D. Carter, X. Wang, and M. Krumpelt, *J. Electrochem. Soc.*, **146** (4), 1273 (1999).

5. C. Xia, F. Chen and M. Liu, *Electrochemical and Solid-State Letters*, **4** (5) A52 (2001).

6. C. Wang, W. L. Worrell, S. Park, J. M. Vohs, R. J. Gorte, *J. Electrochem. Soc.*, **148** (8), A864 (2001).

7. S. J. Visco, C. P. Jacobson, and L. C. De Jonghe, U.S. Pat. No. 6458170, (October 1, 2002).

8. H. Uchida, S. Arisaka, and M. Watanabe, *J. Electrochem. Soc.*, **149** (1), A13 (2002).

9. S. B. Adler, *Chem. Rev.,* **104**, 4791 (2004)

10. M. Watanabe, H. Uchida, M. Shibata, N. Mochizuki, and K. Amikura, *J. Electrochem. Soc.*, **141**, 342 (1994).

11. S. J. Visco, C. P. Jacobson, and L. C. De Jonghe, U.S. Pat. 6682842, (January 27, 2004).

12. C. P. Jacobson, X. Chen, L. C. De Jonghe, and S. J. Visco, *Ionic and Mixed Conducting Ceramics V*, The Electrochemical Society Proceedings, Pennington, NJ (2004).

13. K. Yamahara, C. P. Jacobson, S. J. Visco, and L. C. De Jonghe, *Solid State Ionics*, **176**, (3-4) 275 (2005).

14. J. M. Ralph, C. Rossignol, and R. Kumar, *J. Electrochem. Soc.*, **150** (11), A1518 (2003).

15. R. A. De Souza, J. A. Kilner, *Solid State Ionics*, **106**, 175 (1998).

16. R. A. De Souza, J. A. Kilner, *Solid State Ionics*, **126**, 153 (1999).

17. T. Shishido, Y. Yamamoto, H. Morioka, K. Takaki, and K. Takehira, *Applied Catalysis A: General*, **263**, 249 (2004).

18. H. Zhao, D. J. Draelants, and G. V. Baron, *Catalysis Today*, **56**, 229 (2000).

19. S. Jung, C. Lu, H. He, K. Ahn, R. J. Gorte, J. M. Vohs, *J. of Power Source*, In press.

20. T. D. Mitchell and L. C. De Jonghe, **78** (1), 199 (1995).

21. S. J. Wu and L. C. De Jonghe, *J. Mater. Sci.*, **32**, 6075 (1997).

22. C. Xia, Y. Zhang, and M. Liu, *Electrochemical and Solid-State Letters*, **6** (12), A290 (2003).

23. C. Tanner, K. Fung, and A. Virkar, *J. Electrochem. Soc*., **144**, 21 (1997).

24. S. Jiang, Y. Leng, S. Chan, and K. Khor, *Electrochemical and Solid-State Letters*, **6** (4), A67 (2003).

25. B. C. H. Steele, K. M. Hori, and S. Uchino, *Solid State Ionics*, **135**, 445 (2000).

26. S. B. Adler, J. A. Lane, B. C. H. Steele, *J. Electrochem. Soc*., **143**, 3554 (1996).

27. T. Kawada, N. Sakai, H. Yokokawa, and M. Dokiya, *Solid State Ionics,* **40/41**, 402 (1990).

28. B. C. H. Steele, *Solid State Ionics*, **75,** 157 (1995).

29. P. J. Gellings and H. J. M. Bouwmeester, The CRC Handbook of Solid State Electrochemistry, CRC Press, Boca Raton, P.481 (1996).

30. S. Carter, A. Selcuk, R. J. Chater, J. Kajda, J. A. Kilner and B. C. H. Steele, *Solid State Ionics,* **53-56**, 597 (1992).

31.T. Horita, K. Yamaji, N. Sakai, Y. Xiong, T. Kato, H. Yokokawa, and T. Kawada, *J. Power Sources*, **106**, 224 (2002).

32. T. Horita, K. Yamaji, N. Sakai, H. Yokokawa, T. Kawada, and T. Kato, *Solid State Ionics*, **127**, 55 (2000).

Figure captions

Fig. 1 XRD patterns of the decomposition products from (a) nitrate precursor (b) urea+nitrate precursor heated at 800^{o}C for 2hrs. (P) Peaks corresponding to perovskite phase.

Fig. 2 The EDX spectrum of an infiltrated particle shown in the embedded TEM image.

Fig. 3 SEM images of a porous LSM-YSZ cathode with infiltrated nano SSC particles and after heated at 700^{o}C for 750hrs (the embedded).

Fig. 4 Performance curves for the cell without (■) and with (□) nano SSC particles in an LSM-YSZ cathode at 600^{o}C (fuel: 97%H_2 + 3%H_2O).

Fig. 5 Impedance plots for the cell without (■) and with (□) nano SSC particles in an LSM-YSZ cathode at 600^{o}C (fuel: 97%H_2 + 3%H_2O).

Fig. 6 Impedance spectra of symmetric LSM-YSZ/YSZ/LSM-YSZ cells (square) with infiltrated nano LSM (circle), SSC (triangle) and LSF (star) at 600^{o}C.

Fig. 7 Simplified extended TPB between YSZ and LSM.

Fig. 8 Total oxygen conductivity multiplied by the oxygen ion diffusion resistance, per unit TPB, in arbitrary units *versus* $\log[\frac{R_2^S}{R_o^{ox}}\text{(cm)}]$.

.

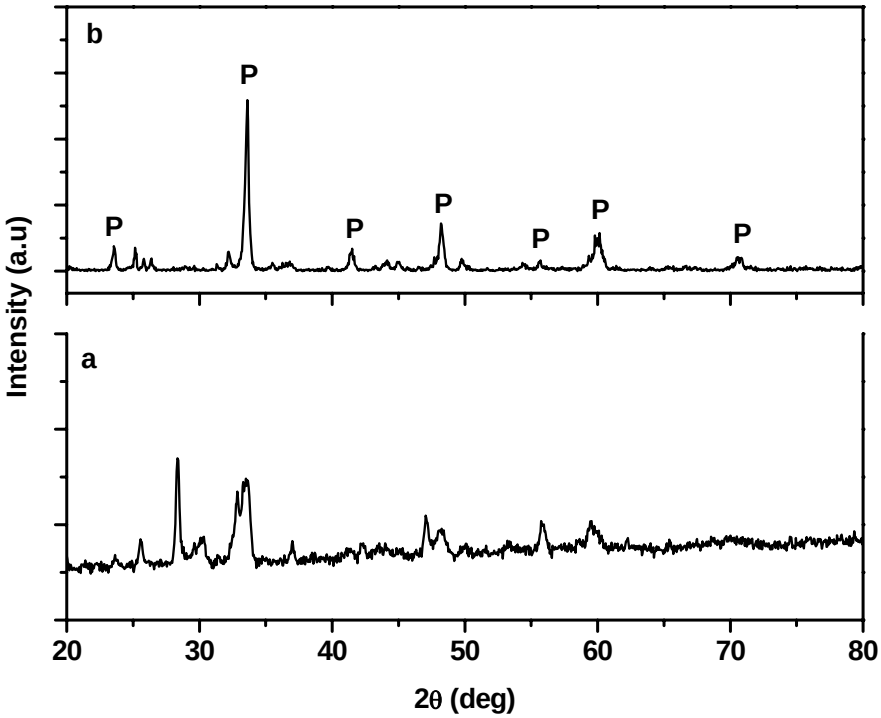

Fig. 1

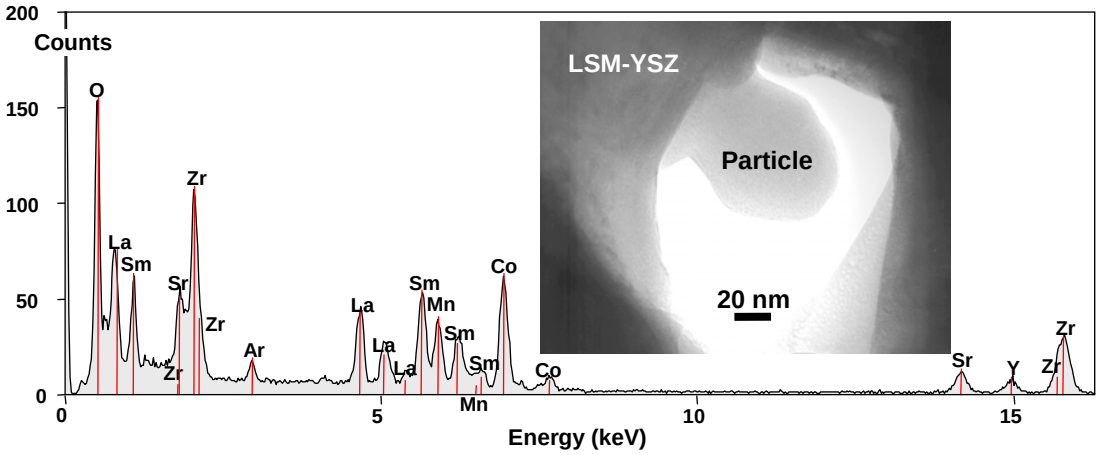
200
Counts
150
100
50
0
0
5
10
15
Energy (keV)
O
La
Sm
Sr
Zr
Ar
Mn
Co
Y
LSM-YSZ
Particle
20 nm

Fig. 2

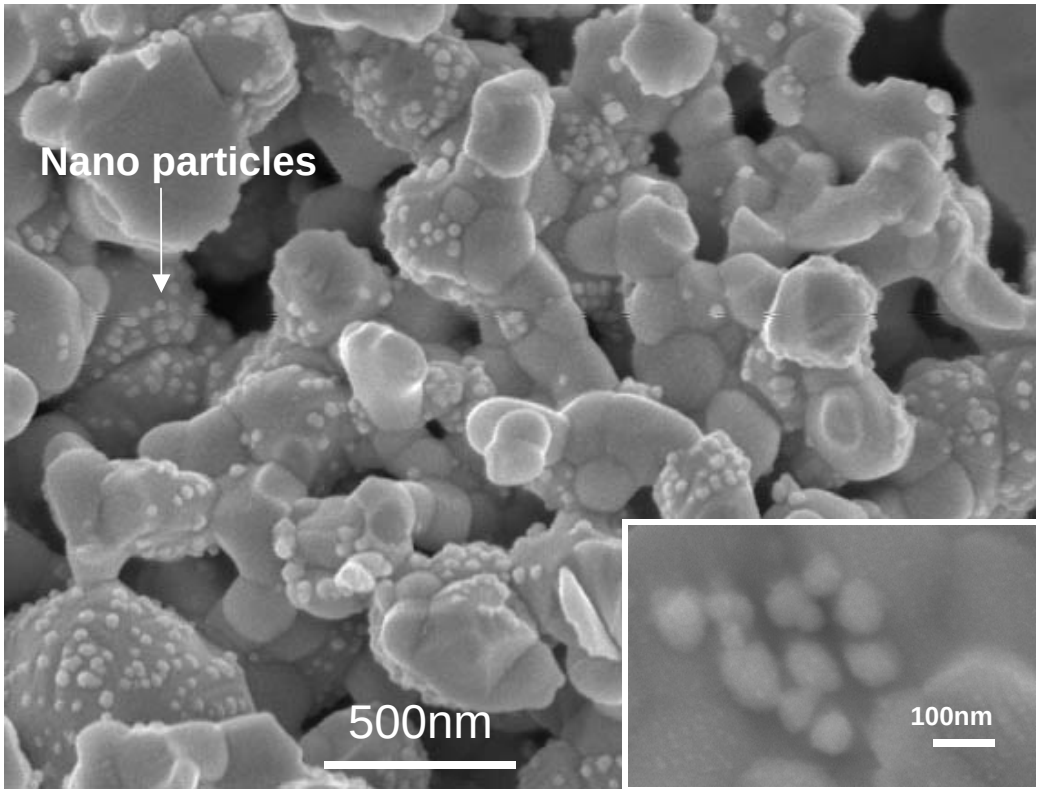

Fig. 3

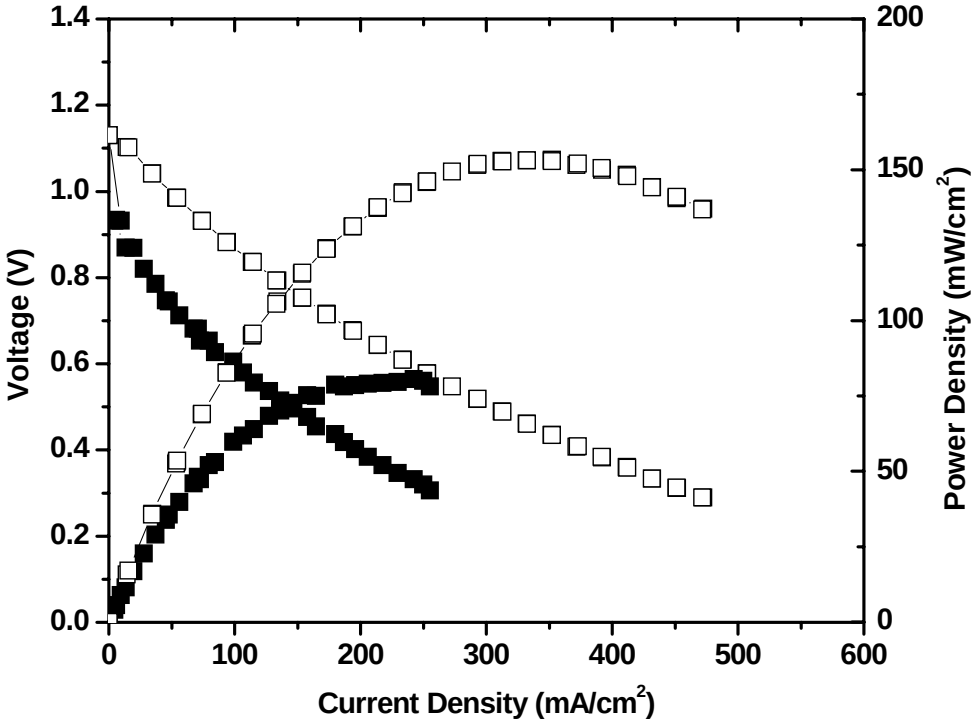
Voltage (V)
Power Density (mW/cm^2)
Current Density (mA/cm^2)
0.0
0.2
0.4
0.6
0.8
1.0
1.2
1.4
0
50
100
150
200
0
100
200
300
400
500
600

Fig. 4

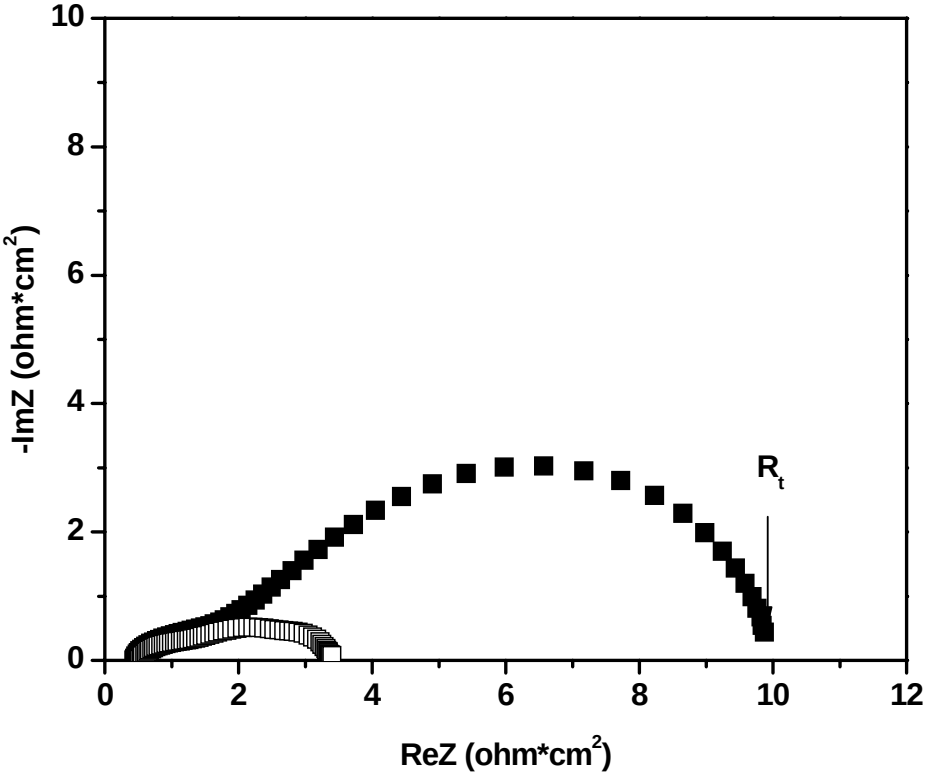

Fig. 5

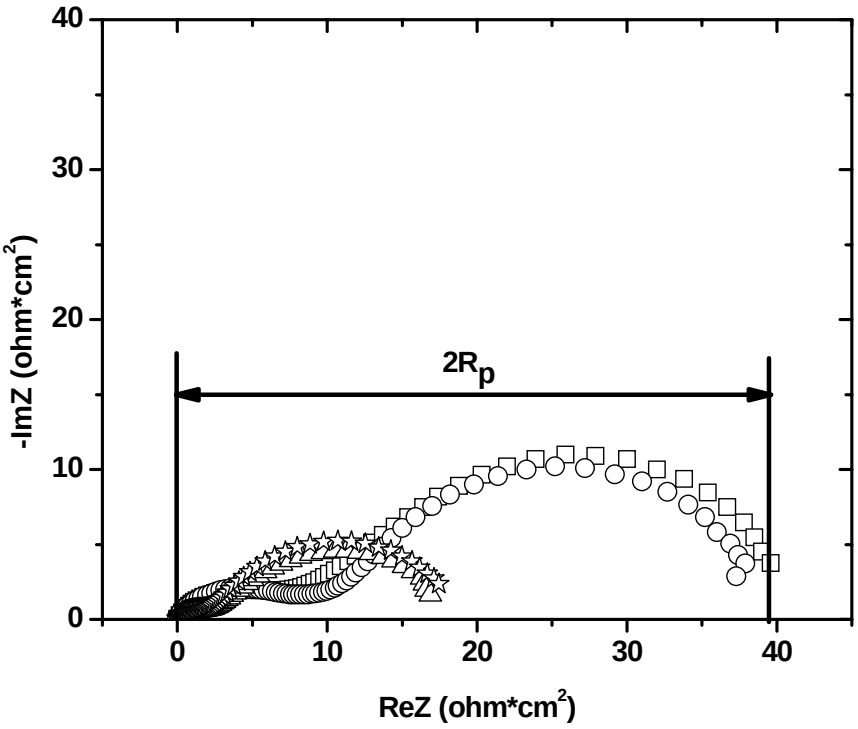

Fig. 6

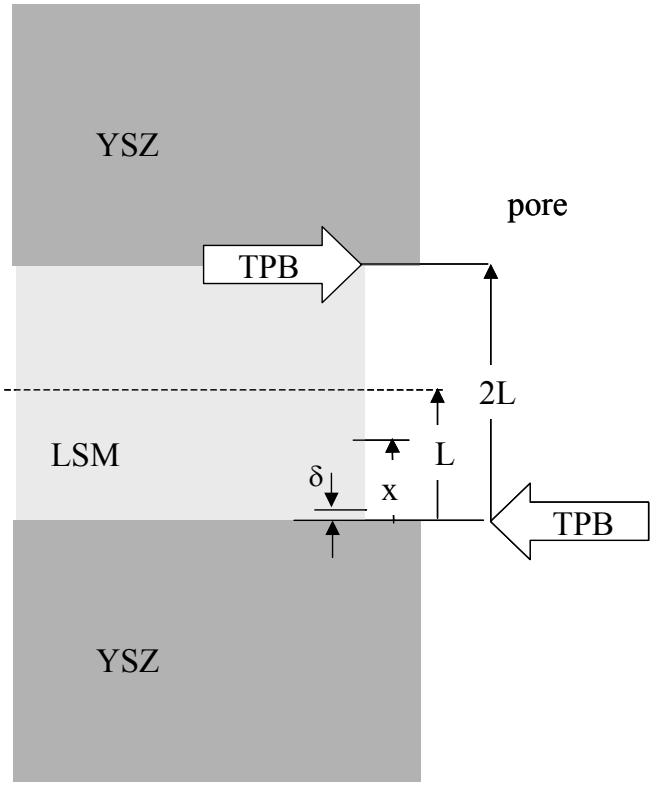

Fig. 7

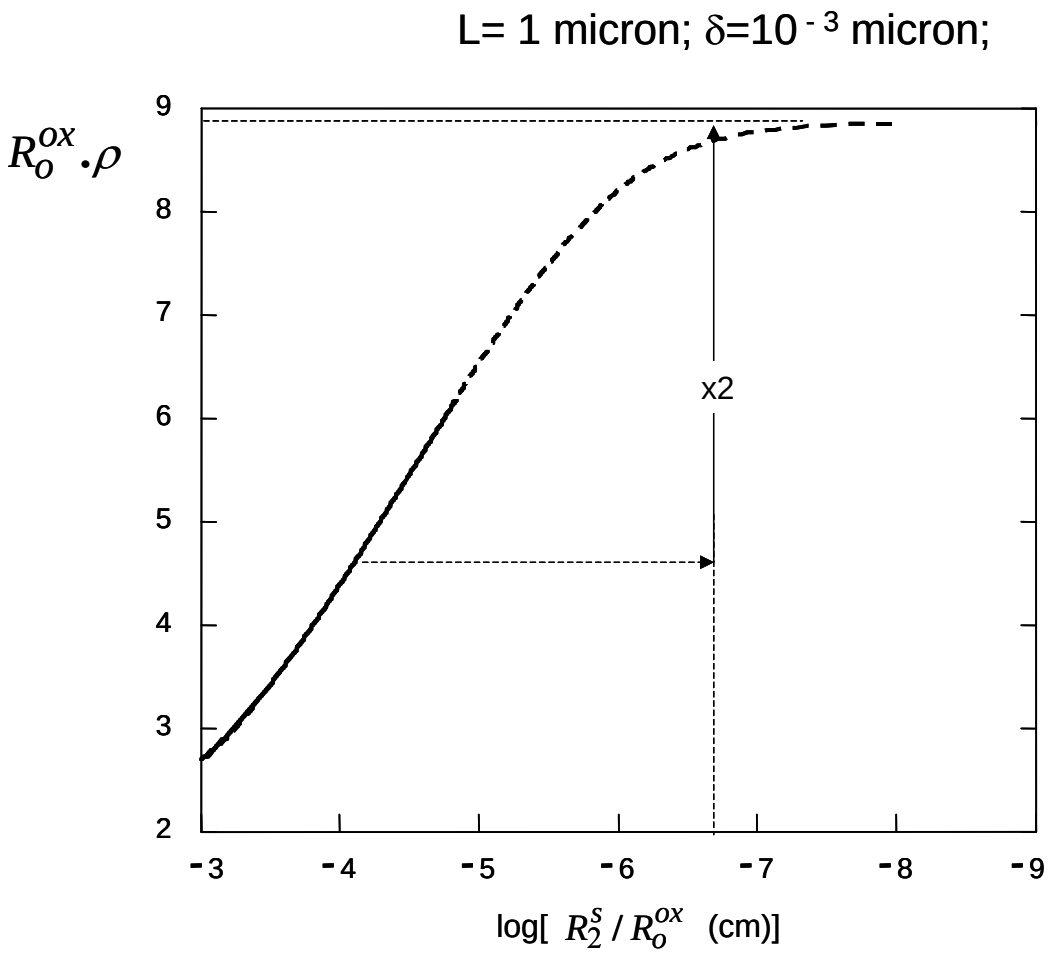
L= 1 micron; δ=10 - 3 micron;
$R_o^{ox} \cdot \rho$
9
8
7
6
5
4
3
2
x2
-3
-4
-5
-6
-7
-8
-9
log[R_2^s / R_o^{ox} (cm)]

Fig. 8